nature communications

Article

https://doi.org/10.1038/s41467-025-59828-6

A generalizable approach for programming protease-responsive conformationally inhibited artificial transcriptional factors

Received: 23 July 2024

Accepted: 6 May 2025

Published online: 17 May 2025

Check for updates

Yinxia Liu, Lingyun Zhao, Jinshan Long, Zhenye Huang, Ying Long, Jianjun He ✉ & Jian-Hui Jiang ✉

Synthetic genetic circuits that harness programmable protein modules and artificial transcription factors (ATF) to devise event-triggerable cascaded pathways represent an essential class of tools for studying cell biology. Fine-tuning the general structural functionality of ATFs is important for constructing orthogonal and composable transcriptional regulators. Here, we report the design of a protease-responsive conformationally inhibited system (PRCIS). By intramolecularly linking the free DNA-binding domains of ATF to confined dimerized regions, the transcriptional binding is conformationally inactivated. The function of DNA binding is reinstated upon proteolytic cleavage of linkages, activating the downstream gene expressions. The versatility of PRCIS design is demonstrated through its adaptability to various ATFs and proteases, showcasing high activation ratios and specificity. Furthermore, the development of PRCIS-based triple-orthogonal protease-responsive and dual-orthogonal chemical-inducible platforms and Boolean logic operations are elaborated in this paper, providing a generalizable design for synthetic biology.

Modular protein designs that fine-tune their structural activity to develop genetically encodable circuits have emerged as versatile tools for biochemical signaling, transcription activation, and protein trafficking[1–3]. One or multiple stimuli-responsive protein modules that are conditionally activated under light illumination, small-molecule induction, or protease cleavage are often employed to realize precise regulation over synthetic signaling pathways[4–6]. Among those, artificial transcription factors (ATFs) are core elements of customized circuits responsible for signal output and event transformation, providing high signal-to-noise ratio, orthogonal genetic activation, and long-lasting and cascadable transmission[7]. So far, ATF-equipped synthetic circuits, including ChaCha[8], MESA[9], and synNotch[10], have found notable applications in synthetic biology and cell biology. For example, the engineered synNotch receptor that senses the tumor-specific antigen to cleave the intracellular ATF cargo for effector expression has shown promise in the development of novel chimeric antigen receptor T cells[11]. Future advances in this field aim to create modular synthetic circuits capable of processing multiple interactions concurrently, with a focus on developing generalizable, and programmable strategies with higher orthogonality.

To avoid potential endogenous transcriptional interference, ATFs used in building genetic circuits for mammalian cells are predominantly sourced from bacterial or yeast origins[12]. These ATFs are characterized by DNA-binding domains (DBD) and activation domains[13]. For example, the homodimer yeast GAL4 is a widely adapted ATF containing binuclear cluster domains to bind the upstream activation sequence (UAS) for gene activation in mammalian cells and live animal models[14]. Routine implementation of ATF-coupled genetic circuits relied on the anchoring of ATF to the intracellular membrane to spatially keep the ATF from activating the nuclear gene transcription, thereby rendering these circuits applicable solely to signaling membrane-associated dynamics[15–17]. Structurally tuning the activity of

Affiliated XiangTan Central Hospital of Hunan University, College of Chemistry and Chemical Engineering, School of Biomedical Sciences, Hunan University, Changsha 410082, China. ✉e-mail: jianjunh@hnu.edu.cn; jianhuijiang@hnu.edu.cn

ATFs can further enpower the versability of genetic circuits. Conformational regulations of protein fluorescence[18] and peroxidase activity[19] have been demonstrated previously. For example, the FlipGFP[20] utilizes an antiparallel E5/K5 heterodimer to flip the GFP β10 and β11 strands into a parallel structure to suppress the assembly of full-length GFP. By incorporating a protease cleavable peptide (PCP) of *tobacco etch virus* protease (TEVp), the fluorescence recovery of FlipGFP can be used to report TEVp activity.

Such protease-responsive designs are advantageous for their fast and precise activation, versatile conformational and transformational changes, and high genetic encodability and integration[21–23], and play key roles in the engineering of artificial proteins and circuits[24,25]. For example, the recently reported "synpoptosis" circuits employed protease switches to dictate cell death pathway[26]. However, when programming protease-responsive transcriptional activation, previous studies focused on controlling the proximity of membrane-anchored ATFs with proteases[27] or split proteases[28], or proteolytically removing of inhibiting domain[29] or degrading[30] of ATFs. Despite these advances, there has been limited exploration of structurally tuning the activities of ATFs with protease switches.

Here, we develop a generalizable protease-responsive conformationally inhibited system (PRCIS) that enables orthogonal control over ATF activity through protease-induced restoration of constrained conformation. After rational design, the DBDs in the general structure of PRCIS are conformationally constrained by linking to rigid dimerizing partners through short peptides, precluding their adaptive interaction with DNA. The cleavage of these peptide links liberates the DBDs, reinstating theirs strong binding to DNA promoters with concurrent activation of gene transcription (Fig. 1a). We have successfully generalized PRCIS to different ATFs with responsiveness to different proteases, and engineered PRCIS-based orthogonal reporter systems for multiple proteases and chemical inducers. PRCIS-based bioactuators and biosensors exhibit minimal basal activity, composability, and orthogonality, providing an alternative paradigm for regulating ATF activity for synthetic biology applications.

Results

Design GAL4-derived PRCIS

As a proof-of-concept, we embarked on the rational engineering of a conformationally constrained GAL4, in which the DNA binding was incapacitated from structural distortion and could be reinstated by proteolytic cleavage. As revealed by the crystal structure, the full-length GAL4 consisted of a DBD of residues 7–40 (termed GAL4 (7–40)) and a dimerization domain of GAL4 (50–94) (Fig. 1b)[31]. The dimerized region started at residue 50 with the first helix GAL4 (51–71) forming a typical coiled-coil, and GAL4 (1–65) can bind DNA with a much lower affinity[32]. These truncated GAL4 (tGAL) structures are often fused to engineered functional components to construct biosensors that respond to light or ligand induction[33–35]. Therefore, we designed a series of tGAL-derived conformationally constrained variants with residues 1-50, 1-65, and 1-70 (Fig. 1c). In order to stabilize the tGAL homodimer, the high-affinity E5/K5 coiled-coil dimerizing peptides[36] were linked to the truncated position, generating the E5/K5-extended tGAL (eGAL). The introduction of E5/K5 greatly enhanced the dimerization of GAL4 (1-50) and GAL4 (1-65) with improved transcription activation, as validated by the GAL4/UAS-encoded mCherry reporter that transiently transfected into HEK293T cells (Supplementary Fig. 1).

Considering that the flexibility of the DBDs was critical for their adaptive contacting to the DNA promoters, we introduced conformation constraints in the DBDs by linking the N-terminal of one DBD to the E5 with a PCP of TEVp (TEVpcp), generating an intramolecularly half-opened, half-cleavabled eGAL (see $eGAL^{o/+}$ in Fig. 1d and Supplementary Fig. 2). The engineered $eGAL^{o/+}$ exhibited significantly increased expression of the mCherry reporter in response to TEVp, but the background fluorescence was unfavorably high. Alternatively, an intermolecularly half-opened, half-locked eGAL was constructed by constraining the DBD to E5/K5 through the spontaneous assembling of GFP β1-10 and β11 (see $eGAL^{+/o}$ in Fig. 1d and Supplementary Fig. 3)[37]. Similar fold improvements were observed between $eGAL^{o/+}$ and $eGAL^{+/o}$, suggesting the constraining of DBD can be achieved via both intramolecularly linking and intermolecularly tethering. To improve the protease activation ratio, we sought to enhance the structural distortion by engineering more variants in which the other free DBD was conformationally constrained with a protease uncleavable peptide (see $eGAL^{-/+}$ and $eGAL^{+/-}$ in Fig. 1d and Supplementary Figs. 4, 5). In this case, the background signals were dramatically reduced, indicating potent transcription inhibition from this dual-constraining strategy. However, the untieable constraint also compromised the transcription activation, resulting in reporter intensity reduction. Hence, we further engineered the dual PCP-locked eGAL ($eGAL^{+/+}$, in Fig. 1d and Supplementary Fig. 6). As expected, this design displayed the highest enhancement folds with minimal background fluorescence. We also found that eGAL (1-70)-based designs, exhibited improved reporter intensity than eGAL (1-50) and reduced background fluorescence than eGAL (1-65)-derived designs, suggesting that the first helix was beneficial for maintaining the conformational rigidity and increasing the structural constraint. Therefore, the eGAL (1-70)-derived $eGAL^{+/+}$ was used as the optimal PRCIS design of GAL4 in all subsequent experiments. Notably, effective constraining was only observed by fusing GFP β1-10 to the DBD, not GFP β11 (Supplementary Fig. 7a and b), presumably due to the constraint-limited assembly of GFP β1-10 and β11. Additionally, as an indicative result of proteolytic activation of $eGAL^{+/+}$, the fluorescence of the assembled split GFP decreased markedly (Supplementary Fig. 7c). Finally, we shown that TEVp alone induced no mCherry transcription (Supplementary Fig. 7d).

We further looked into the impact of E5/K5 extension by comparing $eGAL^{+/+}$ with the non-extended tGAL-derived PRCIS designs, in which the DBDs of tGAL (1-70), tGAL (1-96), tGAL (1-106) and tGAL (1-147) were directly constrained to the truncated dimerized domains in a similar manner to $eGAL^{+/+}$ (denoted as $tGAL^{+/+}$ Supplementary Fig. 8a). Notably, while poor fluorescence enhancement was observed for $tGAL^{+/+}$ (1-70) design, other $tGAL^{+/+}$ derivatives demonstrated even stronger reporter intensity compared to $eGAL^{+/+}$. However, these $tGAL^{+/+}$ also exhibited higher background signals as compared to $eGAL^{+/+}$, especially for $tGAL^{+/+}$ (1-106) and $tGAL^{+/+}$ (1-147). This increased background is likely attributable to the flexibility conferred by the GAL4 (96-147) (Supplementary Fig. 8b). To gain more insights into the structure of PRCIS, we performed structure prediction for the protein sequences using the open-source Alphafold2[38]. After 12-round simulation, the generated model of $eGAL^{+/+}$ was consistent with our design, in which the DBDs are upper-flipped from the DNA-binding conformation (Supplementary Fig. 9). Finally, the performance of $eGAL^{+/+}$ is validated in different cell lines (Supplementary Fig. 10), along with its ability to activate the transcription of other proteins, including the secreted embryonic alkaline phosphatase (SEAP), interleukin 2 (IL-2), and Interferon gamma (IFN-γ) (Supplementary Fig. 11).

To assess the performance of PRCIS, we compared it to the commonly employed membrane-tethered ATFs (Fig. 2a). Appreciable background mCherry fluorescence was detected for the membrane-bound GAL4 (1-147) and GAL4 (1-96) (Fig. 2b, c), likely ascribed to the leaky translocation of GAL4 from the membrane into the nucleus. Lower level of TEVp-mediated mCherry expression was observed for GAL4 (1-70). In contrast, greatly reduced background fluorescence was observed for $eGAL^{+/+}$. As a result, even the activated reporter signal of $eGAL^{+/+}$ is weaker than GAL4(1-147), it displayed the highest improvement fold (396-fold) upon TEVp induction, manifesting the advantage of PRCIS for transcriptional programming that require background suppression. Interestingly, in the absence of TEVp, the subcellular distribution of $eGAL^{+/+}$ is predominantly localizes to the cytosol

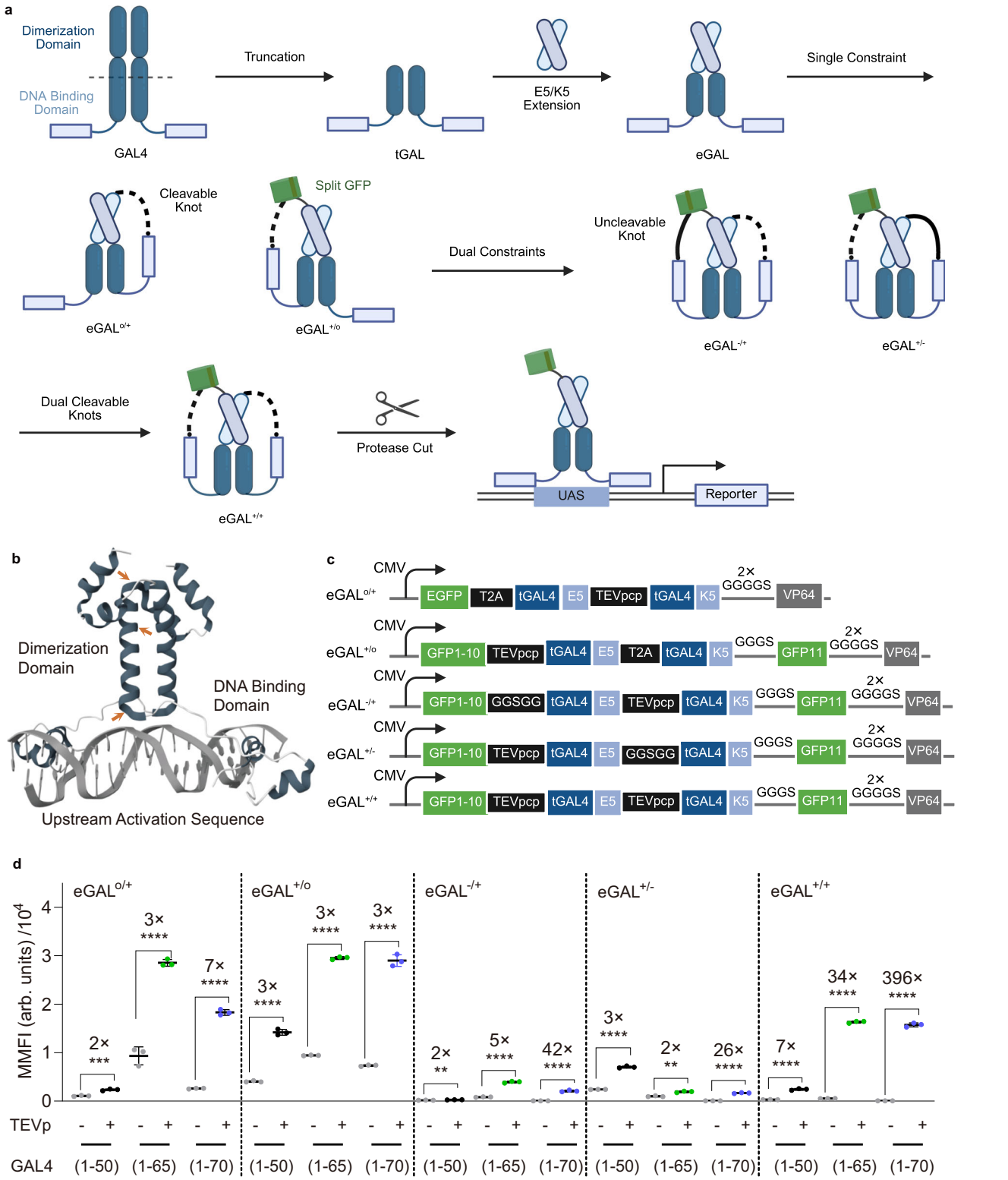

(Supplementary Fig. 12a), presumably attributed to the inhibition of the nuclear localization signal of eGAL$^{+/+}$ by conformationally constraints[39]. In contrast, TEVp-induced cleavage triggered significant nuclear translocation of eGAL$^{+/+}$, evidenced by a 2.2-fold increase in the nucleus-to-cytosol fluorescence ratio (0.39 ± 0.11 vs 0.18 ± 0.12; $p < 0.0001$, Supplementary Fig. 12b). As a reference, the calculated nuclear localization efficiency of the unmodified GAL4 (1-147) is 0.53.

Prior to integrating the optimized eGAL$^{+/+}$ into genetic circuits, it is critical to assess its binding specificity. To this end, we performed a genome-wide comparative analysis between eGAL$^{+/+}$ and the unmodified GAL4 (1-147) using the CUT&Tag technology[40,41]. The results revealed negligible differences in the genomic distribution of the enriched binding peaks and the transcriptional start site (TSS)-associated signal profiles between eGAL$^{+/+}$ and GAL4 (Supplementary Fig. 13a, c). Notably, the highest enriched regions harbored multiple genomic loci containing sequences (CGG-N$_m$(m = 9,10,12)-CCG) closely resembling the canonical GAL4-binding motif (Supplementary Fig. 13b). Moreover, sequencing data obtained from eGAL$^{+/+}$ exhibited

Fig. 1 | Design and optimization of GAL4-derived PRCIS. a Schematic illustration of the rational design and optimization of GAL4-derived PRCIS. The dimerization region of GAL4 is first truncated and extended with E5/K5. For single constraint, conformational constraining of DBDs is achieved by fusing one DBD to E5 with a PCP knot (eGAL$^{o/+}$), or tethering the other DBD with a PCP knot to K5 via the assembly of GFP β1-10 and GFP β11 (eGAL$^{+/o}$). Then, the other free DBD is constrained with a protease uncleavable peptide, generated eGAL$^{-/+}$ and eGAL$^{+/-}$. Finally, a dual PCP-locked variant is engineered (eGAL$^{+/+}$). Upon protease-induced PCP cleavage, eGAL$^{+/+}$ will restore the DNA binding and activate reporter transcription. **b** Crystal structure of GAL4 (1-99) binding with DNA (PDB entry: 3COQ). Orange arrows indicate the truncated positions between residues 50 and 51, 65 and 66, and 70 and 71. **c** Constructs of conformationally constrained eGAL designs. For eGAL$^{+/o}$, the two protein fragments are expressed separately using an T2A sequence from a single plasmid, which are then intermolecularly assembled into the dimerized ATF. **d** Evaluating the TEVp-responsive performance of different conformationally inhibited eGAL designs. $n = 3$, individual data points represent independent triplicates performed on the same day. Error bars represent mean mCherry fluorescence intensity (MMFI) in arbitrary units (arbs.units) ± standard deviation (SD). Significance (two-tailed, unpaired t test) and TEVp-induced fold changes of mCherry fluorescence are labeled for each comparison, $^{**}p < 0.01$, $^{***}p < 0.001$, $^{****}p < 0.0001$. **a**, **c** Created in BioRender. He, J. (2025) https://BioRender.com/t0g6x4h. Source data are provided as a Source Data file.

strong correlation with GAL4 datasets (Pearson's R = 0.86; Supplementary Fig. 13d), with 87% of eGAL$^{+/+}$ peaks overlapping with GAL4 (Supplementary Fig. 13e). These results suggested that the structural engineering in eGAL$^{+/+}$ did not affect the DNA-binding specificity of the unmodified GAL4.

We further programmed the PRCIS to express functional proteins capable of modulating cell behaviors, such as T cell activation and cancer cell pyroptosis. First, PRCIS that encoded two single-chain fragment variables (scFv) against CD3 and CD8 receptors (denoted as aCD3 and aCD28) as the secreted reporters were transfected into HEK293T cells. In which, the co-activation of CD3 and CD28 by aCD3 and aCD28 could stimulate the co-cultured Jurkat T lymphocytes cells to secrete IL-2[42] (Fig. 2d). As expected, the presence of both eGAL$^{+/+}$ and TEVp resulted in a marked increase in IL-2 secretion compared to controls (Fig. 2e). Second, we have encoded PRCIS to express the N-terminal domain of gasdermin D (n-GSDMD), which is known to form membrane pores that facilitate pyroptosis[26] (Fig. 2f). The results showed a significant increase in the percentage of lactate dehydrogenase (LDH) release and apoptotic cells in MCF-7 cells transfected with both eGAL$^{+/+}$ and TEVp (Fig. 2g, h). Overall, these experiments demonstrated the applicability of PRCIS across diverse biological contexts.

Engineering chemically inducible eGAL$^{+/+}$ activation

We then explored the application of PRCIS platform to sense chemical inducers through the combination of eGAL$^{+/+}$ with chemical-inducible protein dimerization (CID)[4,43]. As a proof-of-concept, we employed the split nTEVp/cTEVp and nTVMVp/cTVMVp[24,44] and fused them to the well-studied rapamycin (RAP)-inducible dimerization system of FKBP and FRB[45], in which the RAP inducer could restore the TEVp activity, triggering the protease-mediated switch-on of eGAL$^{+/+}$. And we evaluated the performance between fusing eGAL$^{+/+}$ with the split protease and independently expressing eGAL$^{+/+}$ (Supplementary Fig. 14a). We found that fusing eGAL$^{+/+}$ to nTEVp displayed the highest report improvement for the split TEVp system (Supplementary Fig. 14b, c), and expressing eGAL$^{+/+}$ separately exhibited higher enhancement for the split TVMVp system (Supplementary Fig. 14d, e). Overall, the engineered RAP-inducible reconstitution of FRB-cTEVp and FKBP-nTEVp-eGAL$^{+/+}$ displayed the highest signal improvement (Fig. 3a). And this circuit exhibited dose-dependent reporter fluorescence versus RAP concentrations with a half maximal effective concentration (EC50) of 6 nM with up to 122-fold enhancement (Fig. 3b and Supplementary Fig. 15a, b). We further engineered the abscisic acid (ABA)-inducible eGAL$^{+/+}$-based circuit using the dimerization system of ABI and PYL1[46] by adapting a similar design, and achieved an EC50 of 1.4 μM for ABA with 55-fold enhancement (Fig. 3c and Supplementary Fig. 15c, d).

Next, we examined the performance of this chemically inducible eGAL$^{+/+}$ activation within the modular extracellular sensor architecture (MESA) system, a well-established transcriptional circuit designed to report the ligand-induced dimerization of synthetic receptors[47]. In this context, we employed the RAP-induced dimerization system of FKBP and FRB as the extracellular dimerization domain[48] to trigger the intracellular complementation of nTEVp and cTEVp for the proteolytic release of nTEVp-fused GAL4 or eGAL$^{+/+}$ (Fig. 3d). Consistent with prior studies[49], we observed a high background reporter signal associated with the GAL4-based MESA in the absence of RAP (Fig. 3e). In contrast, the incorporation of eGAL$^{+/+}$ resulted in significantly reduced background levels within the MESA framework. While the measured dose-dependent curves displayed similar trends for GAL4 and eGAL$^{+/+}$-reporting systems (Fig. 3f, g), the use of eGAL$^{+/+}$ provided faster response time (2.6-fold at 12 h) with a higher and more reliable fold induction (maximum of 8.3-fold enhancement with $p < 0.001$ at 36 h) of signaling upon the addition of RAP (Fig. 3h, i).

We further exploited eGAL$^{+/+}$ applicability to report endogenous pathways by incorporating it into a G-protein-coupled receptors (GPCR)-based synthetic circuit. GPCR represent the most diverse class of membrane receptors involved in multiple signaling pathways[50], which has been integrated into different synthetic circuits such as Tango[51] and Chacha[8]. By tethering the cTEVp to the C-terminal of human arginine vasopressin receptor 2 (AVPR2), and fusing eGAL$^{+/+}$ and nTEVp to human β-arrestin2, the phosphorylated AVPR2 would recruit β-arrestin2 to re-constitute the active TEVp and subsequently invoke the protease-switched transcriptional program upon ligand activation (Fig. 4a). For comparison, A GAL4-based GPCR circuit was also constructed (Supplementary Fig. 16a). In the absence of AVPR2 agonist vasopressin, substantially reduced background fluorescence was observed for eGAL$^{+/+}$ compared to GAL4 (Fig. 4b). The treatment of vasopressin resulted in a 13.3-fold maximal increase in mCherry fluorescence with an estimated EC50 of 4.1 nM for eGAL$^{+/+}$ (Fig. 4c, d), which demonstrated much higher fold changes than that of the GAL4-based circuit (Fig. 4c and Supplementary Fig. 16b). Moreover, the agonist-induced activation of GPCR signal was inhibited by the treatment with an AVPR2 antagonist VPA-985 with an IC50 of 1.4 nM (Fig. 4e).

Then, we evaluated the potential of chemical-inducible eGAL$^{+/+}$ for drug discovery using the cytosolic PPARγ/RXRα dimerization model system (Fig. 4f). Peroxisome proliferator-activated receptor γ (PPARγ), an important nuclear receptor in human metabolism, was known to potently function in metabolic diseases through ligand-activated heterodimerization with retinoic X receptor α (RXRα), which made PPARγ/RXRα important targets of anti-diabetic drugs[52]. We found that the agonists, GW1929 and Rosiglitazone[53], exhibited dependable activation of mCherry expression with an estimated EC50 of 0.1 and 15 μM, respectively (Fig. 4g, and Supplementary Fig. 17a–d). By contrast, pretreatment of antagonist GW9662 inhibited the agonist-stimulated transcription activation, with a half maximal inhibitory concentration (IC50) of 31 nM and 0.1 μM for GW1929 and Rosiglitazone, respectively (Fig. 4h). Together, these results highlighted the promise of PRCIS platform in programming transcriptional activation system and identifying agonists or antagonists for pharmaceutical targets.

Generalizing PRCIS to protease switches and ATFs

To evaluate the general adaptability of PRCIS design, we then examined the PCP linkers for different proteases in switching eGAL$^{+/+}$. *Hepatitis C*

https://doi.org/10.1038/s41467-025-59828-6

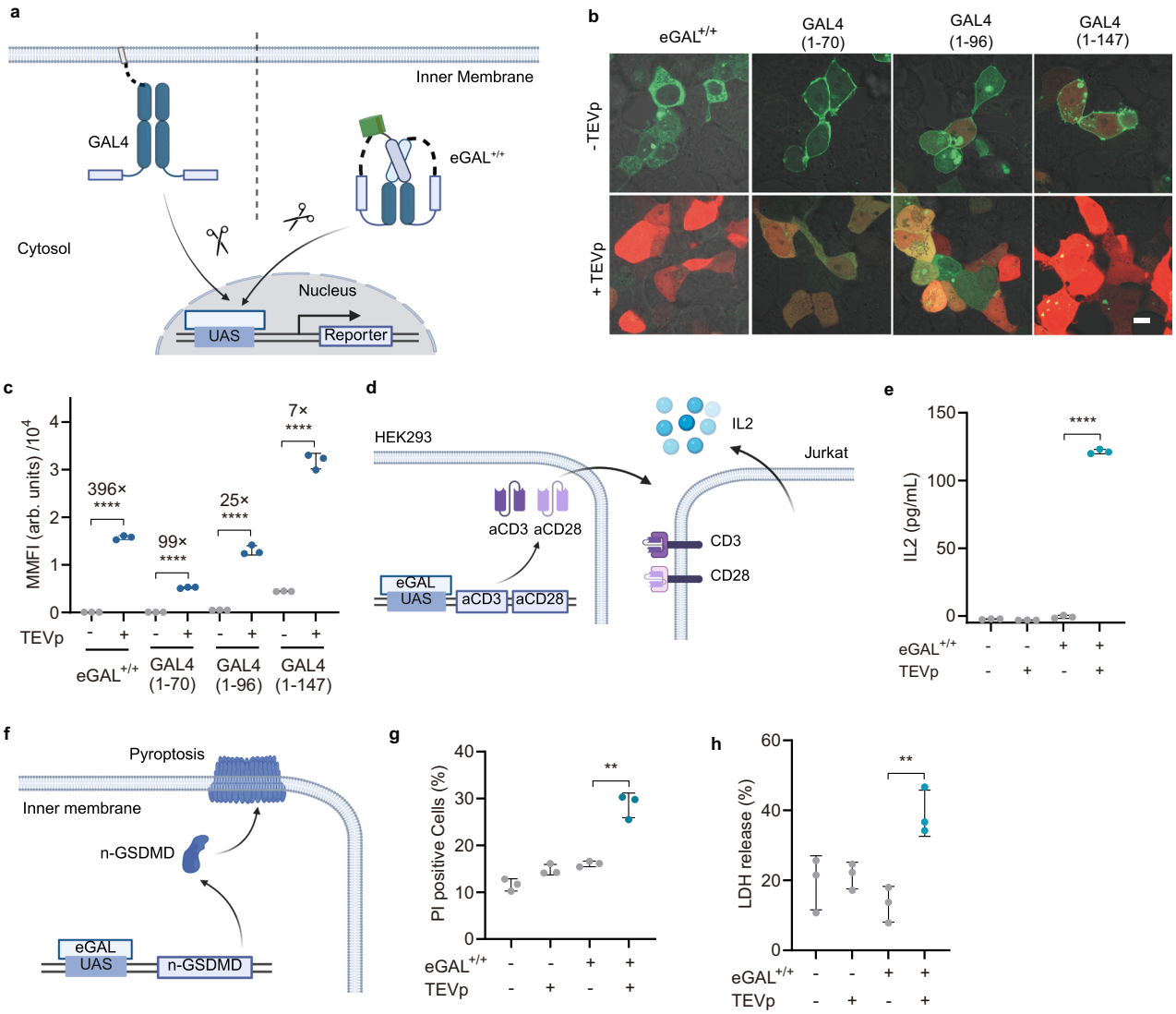

Fig. 2 | Designs of eGAL$^{+/+}$-based reporting systems. a Schematic illustrating the comparison between membrane-anchored GAL4 and cytosolic eGAL$^{+/+}$ in reporting TEVp activity. **b** Fluorescence images and (**c**) statistical analysis of membrane-anchored GAL4 and cytosolic eGAL$^{+/+}$ in reporting protease activity. Merged images of GFP (green), mCherry (red), and bright field are shown, scale bar = 10 μm. TEVp-induced fold changes of mCherry fluorescence are labeled for each comparison. **d** Schematic of activation of Jurkat T cells by TEVp-induced secretion of anti-CD3 scFv and anti-CD28 scFv in eGAL$^{+/+}$ and TEVp co-transfected HEK293 cells. **e** IL2 secretion measured by ELISA (see "Methods"). **f** Schematic of TEVp-induced expression of n-GSDMD triggering cell pyroptosis. Percentages of (**g**) apoptotic cells (see "Methods") and (**h**) LDH release (see "Methods") for MCF-7 cells transfected with eGAL$^{+/+}$ and TEVp. Error bars denote MMFI (arbs.units) ± SD, $n = 3$, individual data points represent independent triplicates performed on the same day. Significance (two-tailed, unpaired t test) is labeled above data, $^{**}p < 0.01$, $^{****}p < 0.0001$. **a**, **d**, **f** Created in BioRender. He, J. (2025) https://BioRender.com/u3mvxcr. Source data are provided as a Source Data file.

virus protease (HCVp), *plum pox virus* protease (PPVp), and *tobacco vein mottling virus* protease (TVMVp), which have been commonly employed with TEVp to construct orthogonal genetic circuits, were validated (Fig. 5a)[54–56]. As shown in Fig. 5b, PPVp, TVMVp and HCVp exhibited 38-, 231-, and 85-fold signal improvement, respectively, demonstrating the generalizability of PRCIS. Additionally, we found that the protease-induced activation fold is greatly depended on the PCP sequence to be cleaved (Supplementary Fig. 18), suggesting optimization of the preferred PCP substrate is required for improving PRCIS performance. All protease-induced activation of reporter signals exhibited dose-dependent profiles versus protease concentrations (Supplementary Fig. 19). Furthermore, high protease specificity was observed between TEVp, PPVp, TVMVp and HCVp with respect to their corresponding PCPs (Fig. 5c and Supplementary Fig. 20). Next, we evaluated eGAL$^{+/+}$ with two different PCP linkers on either sides corresponding to TEVp and TVMVp. As indicated in Supplementary Fig. 21a, a single cut by TEVp or TVMVp would result in half-opened, eGAL$^{o/+}$ or eGAL$^{+/o}$-mimicking forms with significantly increased reporter signals. The complete cut with two proteases further enhanced the reporter transcription. A similar result was obtained for eGAL$^{+/+}$ with two different PCPs corresponding to TEVp and PPVp (Supplementary Fig. 21b).

To further explore the generality of this design, two other eukaryotic transcriptional factors GCN4 and MAX were selected to engineer the PRCIS of GCN4 and MAX (Fig. 5d and Supplementary Fig. 22)[57]. Residues 226-281 from the basic region leucine zipper (bZIP) protein GCN4 and residues 22-107 from the helix–loop–helix (HLH) protein MAX were truncated at different positions and integrated into the eGAL$^{+/+}$ design (Fig. 5e, f)[58,59]. Upon TEVp expression, the optimal PRCIS of TEVp-responsive E5/K5-extended GCN4 (eGCN$^{+/+}$) were identified for the GCN4 (226-258) with 96-fold fluorescence enhancement, and 55-fold for the optimal PRCIS of E5/K5-extended MAX (eMAX$^{+/+}$) with MAX (22-88). Besides, we evaluated the feasibility of the PRCIS design for a heterodimerized transcription factor MAX/MYC (eMAX/MYC$^{+/+}$) by adapting the eMAX$^{+/+}$ structure (Fig. 5g), which

https://doi.org/10.1038/s41467-025-59828-6

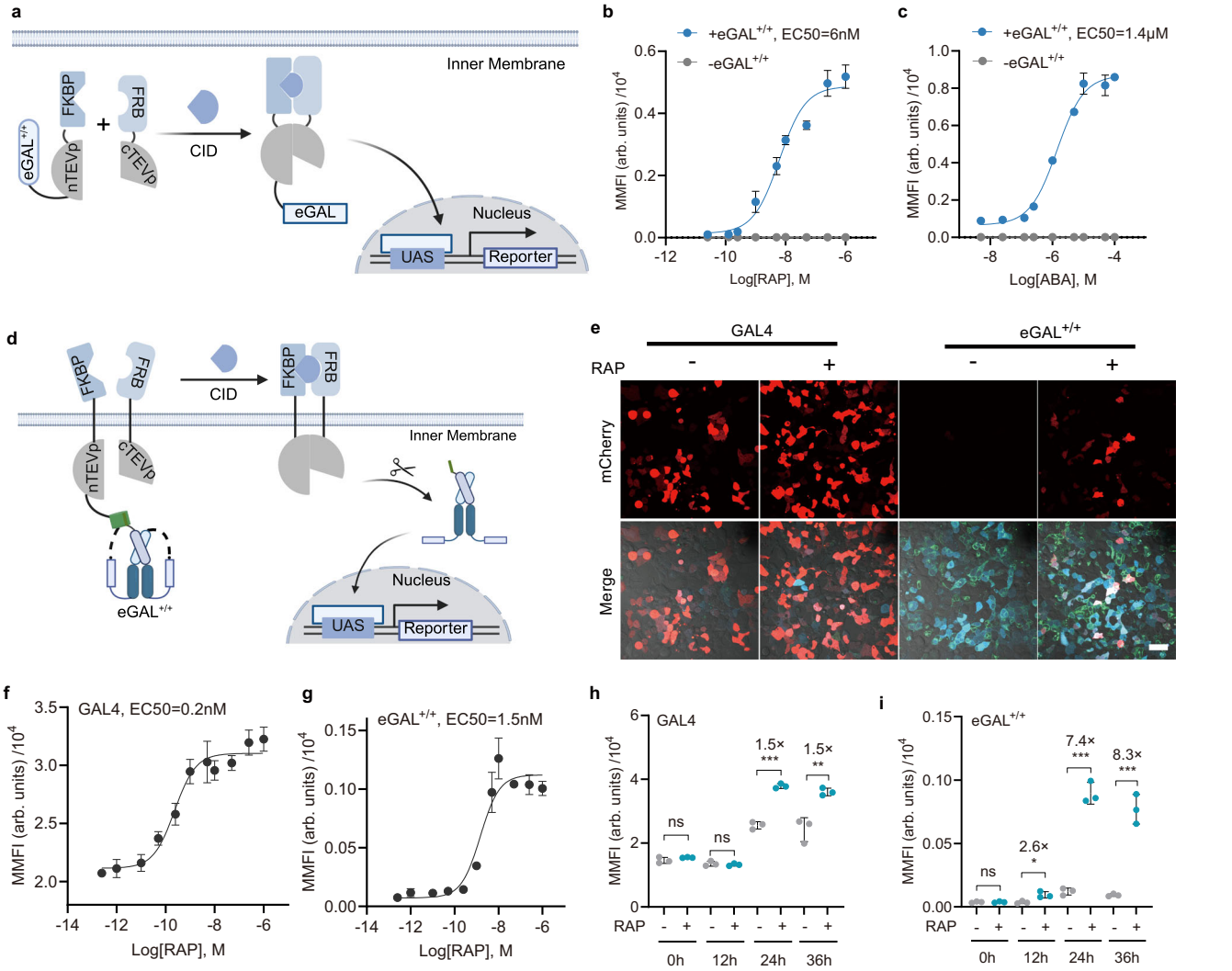

Fig. 3 | Designs of eGAL$^{+/+}$-based CID reporting systems. a Schematic of CID-mediated reconstitution of the split TEVp by dimerization between FRB-cTEVp and FKBP-nTEVp-eGAL$^{+/+}$ for the proteolytic activation of eGAL$^{+/+}$. Dose-response curves of (**b**) RAP-induced dimerization of FRB-cTEVp and FKBP-nTEVp-eGAL$^{+/+}$, and (**c**) ABA-induced dimerization of PYL1-cTEVp and ABI-nTEVp-eGAL$^{+/+}$ for transcription activation of mCherry expression. **d** Schematic of comparison between eGAL$^{+/+}$ and GAL4 in reporting the RAP-induced dimerization of membrane associated FKBP-nTEVp-(eGAL$^{+/+}$ or GAL4) and FRB-cTEVp. Upon RAP induction, the dimerization of extracellular FKBP and FRB would reconstitute the intracellular TEVp for the proteolytic release of membraned anchored eGAL$^{+/+}$ or GAL4. **e** Fluorescence images of reporter expression before and after RAP induction. Merged images of BFP (cyan, BFP plasmid was co-transfected as a control), GFP (green), mCherry (red), and bright field are shown. Scale bar = 50 μm. Dose-dependent profiles of RAP-induced reporter expression using (**f**) GAL4 or (**g**) eGAL$^{+/+}$-based MESA. RAP-induced mCherry expression at 0, 12, 24, and 36 h post RAP incubation from (**h**) GAL4 or (**i**) eGAL$^{+/+}$-based MESA. Error bars denote MMFI (arbs.units) ± SD, $n = 3$, individual data points represent independent triplicates performed on the same day. Significance (two-tailed, unpaired t test) and RAP-induced fold changes of mCherry fluorescence are labeled for each comparison. ns: not significant, $^{*}p < 0.05$, $^{**}p < 0.01$, $^{***}p < 0.001$. **a**, **d** Created in BioRender. He, J. (2025) https://BioRender.com/wxg3f87. Source data are provided as a Source Data file.

afforded a desirable SNR of 42-fold. All PRCIS designs exhibited low background, which resulted in excellent signal enhancement, demonstrating the general adaptability of PRCIS in protease-mediated regulating dimeric transcription factors with α-helix dimerizing region.

Finally, we investigated the generalizability of the dimerizing partners by substituting the split GFP β1-10/11 pair with P3/AP4[60] and CC-A/CC-A′[61] (Fig. 5h), two previously identified coiled-coil dimerizing peptide pairs that provided orthogonal interaction toolboxes for the building of various genetic circuit in mammalian cells[62,63]. In comparison to the split GFP, the introduction of both peptide pairs demonstrated comparable performance in terms of reporter strength (Fig. 5i). Noticeably, the background fluorescence increased substantially for both peptide pairs, suggesting that the optimization of dimerizing partners is crucial for minimizing basal signal levels.

We then explored the potential to engineer orthogonal designs for PRCIS in responding to multiplexed inputs. To this end, we first evaluated different combinations of PCPs and ATFs for reporting the corresponding protease activities. These combinations exhibited desirable folds of enhancement for reporting corresponding protease activities except for the PPVp-responsive eGCN$^{+/+}$ (Fig. 6a–c and Supplementary Fig. 23). Hence, we constructed a triplex orthogonal protease-responsive PRCIS platform consisting of the PPVp-inducible eGAL$^{+/+}$, the TVMVp-inducible eGCN$^{+/+}$, and the TEVp-inducible eMAX$^{+/+}$. Desired fluorescence outputs were detected for the correponsing protease input combinations with negligible cross-talking (Fig. 6d), demonstrating excellent orthogonality of the PRCIS design for multiplexed biosensing and regulating. Furthermore, we extended the PRCIS platform for orthogonal reporting of multiple chemical inputs. The ABA-responsive ABI/PYL1 pair was separately

https://doi.org/10.1038/s41467-025-59828-6

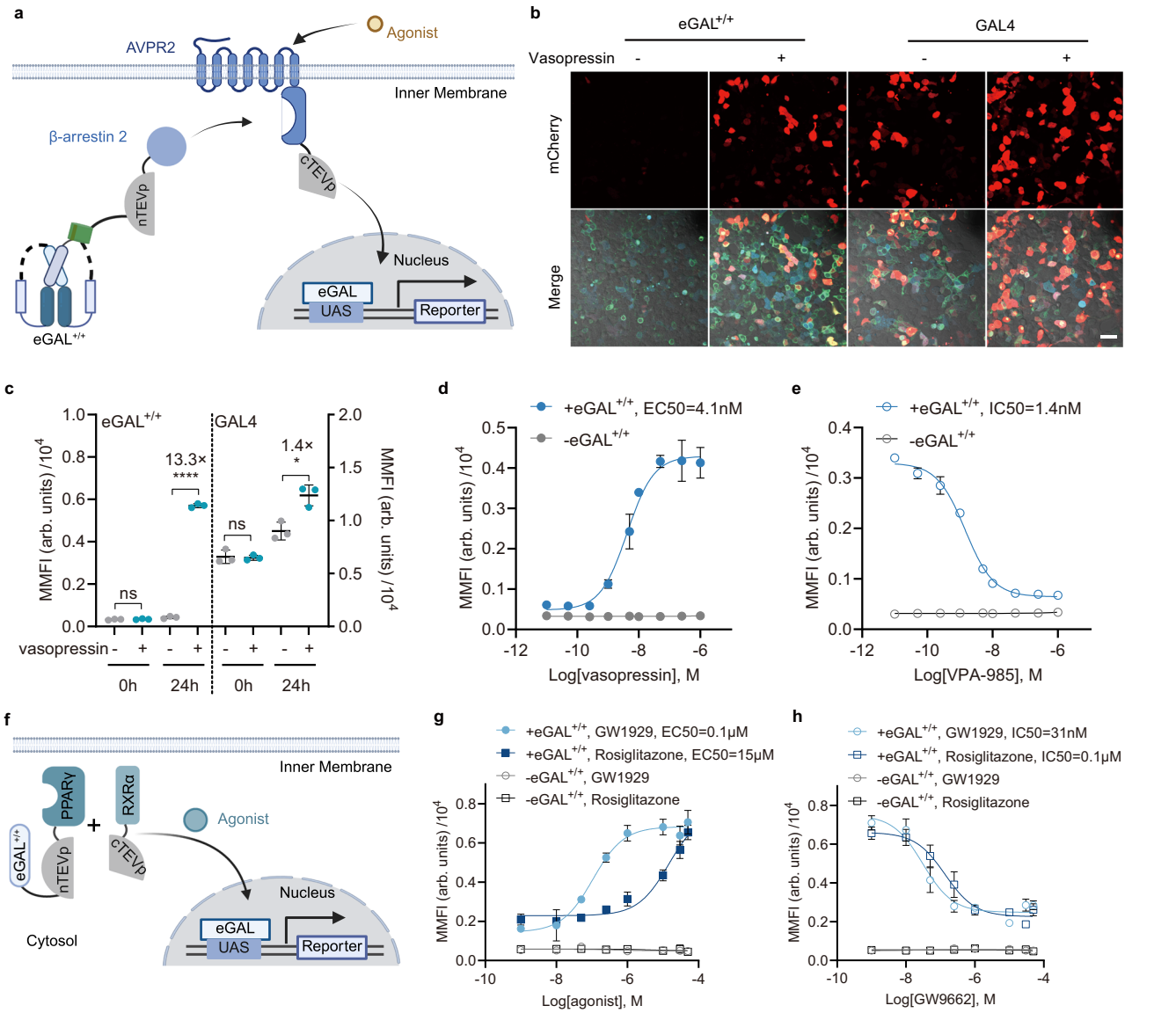

Fig. 4 | Designs of eGAL$^{+/+}$-based biosensors for reporting endogenous pathways. a Schematic of eGAL$^{+/+}$-based GPCR signaling. Upon ligand stimulation, β-arrestin2-nTEVp-eGAL$^{+/+}$ would be recruited to AVPR2-cTEVp to reconstitute TEVp for the proteolytic release of membraned anchored eGAL$^{+/+}$. **b** Fluorescence images of vasopressin-induced reporter expression. Merged images of BFP (cyan, BFP plasmid was co-transfected as a control), GFP (green), mCherry (red), and bright field are shown. Scale bar = 50 μm. **c** Vasopressin-induced fold changes using eGAL$^{+/+}$ or GAL4 to activate reporter fluorescence after 24 h. Fold changes of mCherry fluorescence are labeled for each comparison. Dose-dependent profiles of (**d**) agonist vasopressin-induced and (**e**) antagonist VPA-985-inhibited β-arrestin2 recruitment. For inhibition, 5 nM of Vasopressin was added together with diffirent concentrations of VPA-985. **f** Schematic of eGAL$^{+/+}$-based sensing of cytosolic PPARγ/RXRα dimerization. Dose-response curves of (**g**) agonist-induced dimerization and (**h**) antagonist-inhibited dimerization of eGAL$^{+/+}$-nTEVp-PPARγ and cTEVp-RXRα. GW9662 was added together with 1 μM GW1929 or 15 μM Rosiglitazone. Error bars denote MMFI (arbs.units) ± SD, $n = 3$, individual data points represent independent triplicates performed on the same day. Significance (two-tailed, unpaired t test) is labeled above data, ns: not significant, $^{*}p < 0.05$, $^{****}p < 0.0001$. **a**, **f** Created in BioRender. He, J. (2025) https://BioRender.com/y0i9dcq. Source data are provided as a Source Data file.

fused to nTEVp-eGAL$^{+/+}$ and cTEVp, and the RAP-responsive FKBP/FRB pair was separately fused to nTVMVp and cTVMVp. Upon CID, the reconstituted protease could actively cleave the corresponding PRCIS with the desired downstream expression (Fig. 6e). As validated by the result, RAP or ABA alone precisely induced the corresponding fluorescent protein expression, suggesting the orthogonality for the CID based PRCIS designs.

Next, we investigated the potential to construct the PRCIS-based logic gates with two protease inputs. The 'OR' gate was designed to comprise the TVMVp-responsive eGCN$^{+/+}$ and TEVp-responsive eGAL$^{+/+}$ as well as a reporter plasmid for mCherry expression output with both GCN4 and GAL4 promoters (Fig. 6f). As anticipated, positive mCherry activation was observed in the presence of either TEVp or TVMVp, consistent with the logic of 'OR' gate. The 'AND' gate was designed to comprise a cascade of two PRCIS circuits, exploiting the TEVp-responsive eGAL$^{+/+}$ to activate TVMVp-responsive eGCN$^{+/+}$ expression as the transmitter that promote mCherry expression as the output (Fig. 6g). Indeed, no obvious fluorescence activation was detected in the absence of either TEVp or TVMVp, but the presence of both protease inputs displayed strong mCherry fluorescence, validating the correct function of 'AND' gate. We further engineered an 'INHIBIT' gate which only delivered positive output in the presence of TEVp but no TVMVp (Fig. 6h). The 'INHIBIT' gate was constructed using the TEVp-responsive eGAL$^{+/+}$ with the inert linker to the transcriptional effector

https://doi.org/10.1038/s41467-025-59828-6

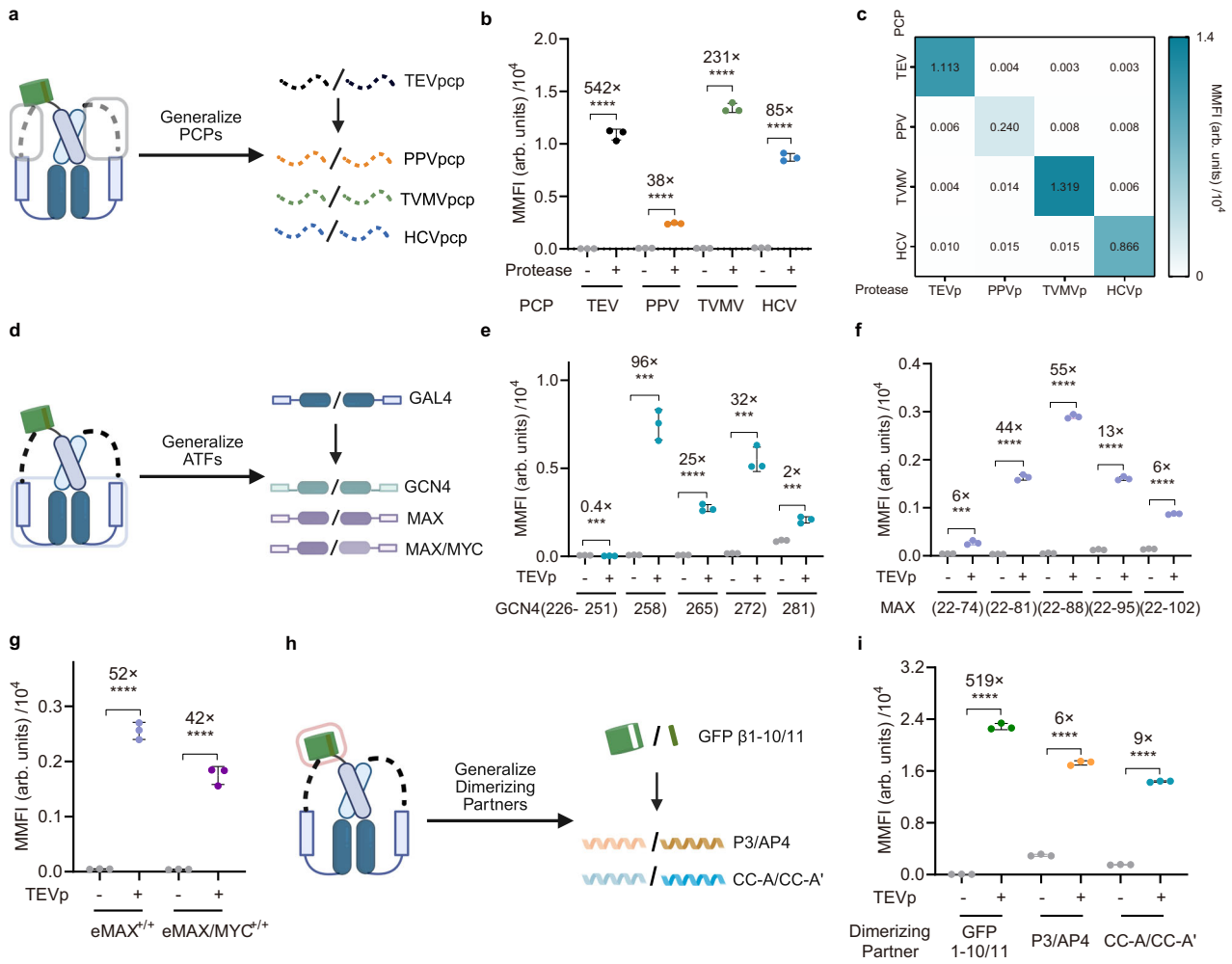

Fig. 5 | Generalizing modules of PRCIS to different proteases, ATFs and dimerizing partners. a Generalizing PCP knots of eGAL$^{+/+}$ from TEVpcp to PPVpcp, TVMVpcp, and HCVpcp. **b** Performance of different proteases in tuning the effectiveness of corresponding PCP-knotted eGAL$^{+/+}$. **c** Protease specificity map of TEVp, PPVp, TVMVp and HCVp in switching on eGAL$^{+/+}$ with TEVpcp, PPVpcp, TVMVpcp and HCVpcp linkers. Protease-induced mCherry intensity are displayed in accordance to a color scale bar. **d** Generalizing ATFs of PRCIS from GAL4 to GCN4, MAX, and MAX/MYC. Performance of TEVp-responsive (**e**) GCN4-derived and (**f**) MAX-derived PRCIS with different truncated lengths. **g** Performance of TEVp-responsive eMAX/MYC$^{+/+}$. **h** Generalizing dimerizing partner of eGAL$^{+/+}$ from split GFP to coiled-coil P3/AP4 and CC-A/CC-A'. **i** Performance of P3/AP4 and CC-A/CC-A' constrained TEVp-responsive eGAL$^{+/+}$. Error bars represent MMFI (arbs.units) ± SD. $n = 3$, individual data points represent independent triplicates performed on the same day. Significance (two-tailed, unpaired t test) and protease-induced fold changes of mCherry fluorescence are labeled for (**b**, **e**, **f**, **g**, **i**). ***$p < 0.001$, ****$p < 0.0001$. **a**, **d**, **h** Created in BioRender. He, J. (2025) https://BioRender.com/axctfb2. Source data are provided as a Source Data file.

VP64 replaced by a TVMVp-responsive PCP linker. As expected, we obtained intense mCherry output only in the situation when TEVp was present but TVMVp was absent. Together, these results confirmed the facile engineering of PRCIS-based Boolean operations.

Discussion

The interaction between ATF and DNA requires conformational flexibility of the DBDs to form effectively complementary interfaces. Previous attempts on regulating ATF activities focus on controlling ATF dimerization through chemical[46,64] or light[33], inhibiting or destabilizing ATFs through effector domains[65] or proteolytic degrons[66]. We propose a different strategy for the structural engineering of ATFs to enable fine tuning of their activities. By conformationally constraining the DBDs of ATFs to the introduced rigid dimerizing domains, the transcriptional binding is inhibited, resulted in greatly reduced background and therefore high fold enhancement of reporter signal. The introduction of high-affinity E5/K5 enhanced the applied constraint so that the promoter-binding is further inhibited, resulting in reduced background fluorescence. A limitation of PRCIS is that it requires two cleavage events to restore full functionality, which may inherently limit the maximum activation potential of ATFs. However, this allows the tuning of expression intensity by selectively unraveling either or both conformationally constraining knots, offering a two-level regulation of expression intensity for synthetic networks.

The ATF activity of engineered PRCIS variants can be conformationally restored upon protease-mediated PCP cleavage, providing readily implementable protease-responsive modules for existing synthetic machineries that harness proteases to transmit cellular stimulation. The versatility of PRCIS-derived molecular circuits is evidenced by their consistent functionality across various mammalian cell types and their ability to express functional preteins for the regulation of cell status. Especially, we have integrated eGAL$^{+/+}$ to establish various CID-responsive biosensors for the reporting of artificial receptor (MESA) and endogenous pathways (GPCR and PPAR). In which, the minimal-background design of PRCIS has demonstrated

https://doi.org/10.1038/s41467-025-59828-6

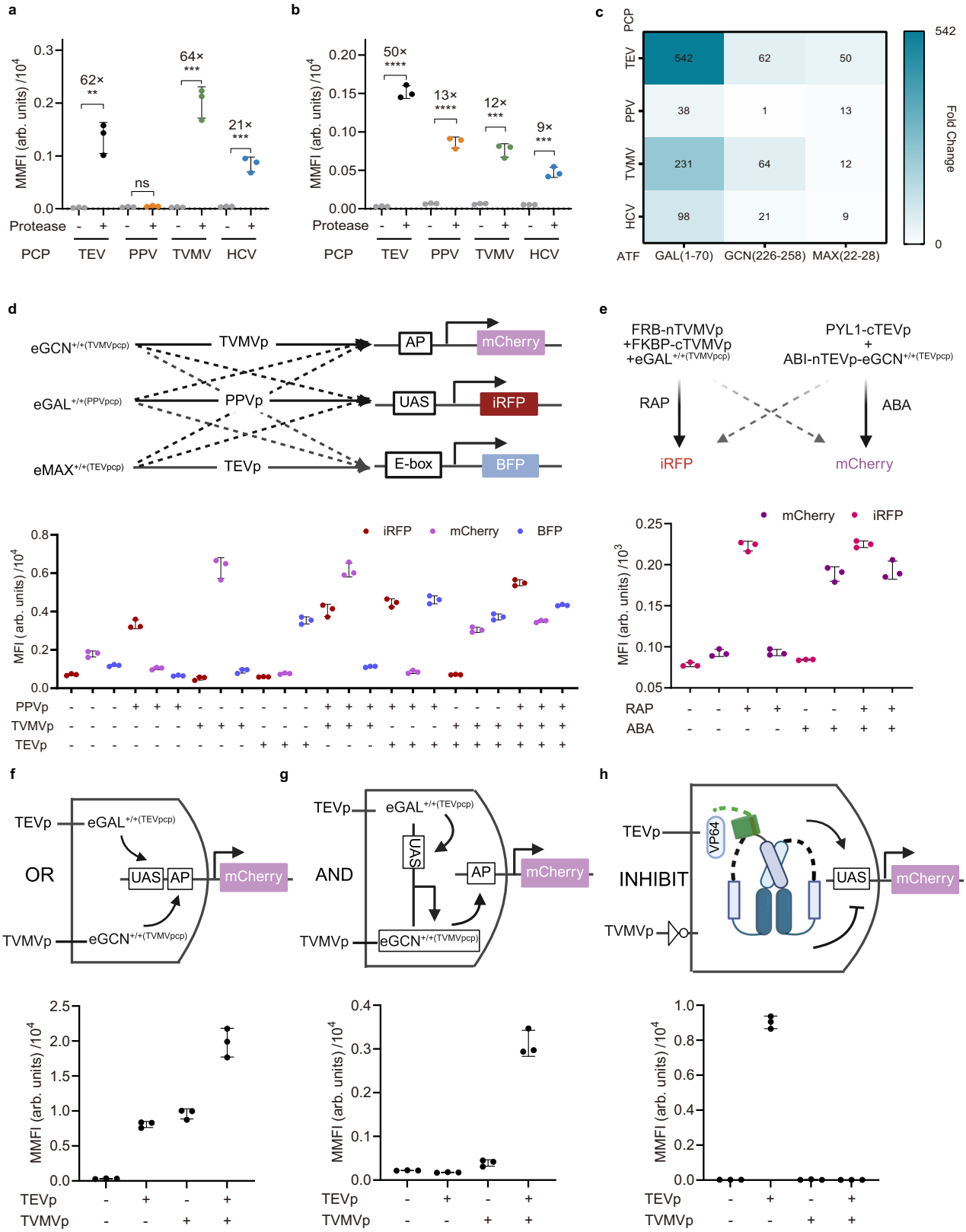

better fluorescence enhancement than conventional membrane-tethered protease-responsive ATF systems which are susceptible to the misexpression of the 'always-on' ATFs in the cytosol and nucleus. As an example, the PRCIS-based approach records GPCR activation with reliable readout than Tango, suggesting that PRCIS is particularly adept at sensitively transmitting low-abundance protease-activation events. Although the proteases validated in this paper are exogenous, we expect its readily transformation into endogenous protease-responsible systems. For example, PRCIS could be modified to visualize the activity of disease-associated proteases, or to respond to tumor-specific proteases to express functional protein for targeted cancer treatment.

ATFs of GAL4, GCN4, MAX are examined and integrated into an combinatorial array of TEVp-, HCVp-, TVMVp-, and PPVp-responsive

Fig. 6 | Design of PRCIS-based orthogonal reporting systems and logic gates. Performance of (**a**) eGCN$^{+/+}$ and (**b**) eMAX$^{+/+}$ with different PCP linkers upon corresponding protease activation. **c** Color map summerizes fold changes of PRCIS equipped with different ATFs and PCPs in respond to corresponding proteases. **d** Schematic illustration and performance of the tri-orthogonal PRCIS-based circuit consisting of TVMVp-inducible eGCN$^{+/+}$ (eGCN$^{+/+(TVMVpcp)}$), PPVp-inducible eGAL$^{+/+}$ (eGAL$^{+/+(PPVpcp)}$) and TEVp-inducible eMAX$^{+/+}$ (eAMX$^{+/+(TEVpcp)}$) for the reporting of all combinations of TEVp, TVMVp, and PPVp inputs. **e** Schematic illustration and evaluation of orthogonal reporting of ABA and RAP with ABA-inducible TEVp-responsive eGCN$^{+/+}$ (eGCN$^{+/+(TEVpcp)}$) and RAP-inducible TVMVp-responsive eGAL$^{+/+}$ (eGAL$^{+/+(TVMVpcp)}$). Schematic illustration and evaluation of PRCIS-based (**f**) 'OR' gate, (**g**) 'AND' gate, and (**h**) 'INHIBIT' gate with TEVp and TVMVp inputs and mCherry outputs. $n = 3$, individual data points represent independent triplicates performed on the same day. For (**d**, **e**), error bars represent MFI (arbs.units) ± SD, For (**a**, **b**, **f**, **g**, **h**), error bars represent MMFI (arbs.units) ± SD. Significance (two-tailed, unpaired t test) is labeled above data, ns: not significant, $^{**}p < 0.01$, $^{***}p < 0.001$, $^{****}p < 0.0001$. Schematic illustrations of (**d**, **e**, **f**, **g**, **h**): Created in BioRender. He, J. (2025) https://BioRender.com/t4qifbc. Source data are provided as a Source Data file.

PRCIS. Noticeably, although these ATFs act in structurally distinctive DNA docking and recognition mechanisms including binuclear cluster zinc binding (GAL4), bZIP (GCN4), or HLH (MAX and MAX/MYC), all DNA-DBD interactions have been effectively disrupted through conformationally tethering, demonstrating the general adaptability of PRCIS design. We anticipate the broad adaption of PRCIS in engineering protease-responsive ATFs, including the large category of bacteria-originated HLH-type ATFs, including TetR, TrpR, and VanR[46]. When generalizing PRCIS to new ATFs, the critical parameter to take into consideration is the truncation positions of ATFs, which greatly affect the applied constraint and conformation recovery. As exemplified in the optimization of GCN4 and MAX-derived PRCIS.

Furthermore, the generalizability of PRCIS enables the modular compositions of multiple independent PRCIS into orthogonal communication frameworks, as demonstrated by the dual-orthogonal chemical inducible circuit and the triple-orthogonal protease-responsive network. Moreover, PRCIS-based logic gates that allows the AND, OR, and INHIBIT operations are established, which lay the foundation for the construction of advanced logic computation circuits. By adapting the orthogonal protease-responsive PRCIS, the expression patterns and levels of different genes can be independently tuned via synthetically programming the relaying and looping modules. This design can be further extended to build PRCIS-based multilayered genetic circuits. Moreover, effective packaging and delivering of multiple plasmid constructs is critical to increasing circuit complexity for developing PRCIS-based multiplexed networks for in vivo applications. We expect that the generalizability and composability of PRCIS can empower designable toolkits for investigating intracellular interactions involving multiplexed pathways.

Methods

Plasmid construction

The construction of all plasmids was carried out by General Biol (Anhui) Co., utilizing techniques such as gene synthesis, direct subcloning or polymerase chain reaction (PCR) to amplify genes and functional domains from an array of donor plasmids or sequences available from Addgene and various references. The complete lists of plasmids are included in Supplementary Data 1-4. All plasmids were constructed using a mammalian expression vector pcDNA3.1(+) or a lentiviral vector pCDH. All plasmids were extracted from *E.coli* cells with QIAprep Spin Miniprep. In the case of reporter plasmids, sequences such as UAS, AP-box, or E-box were integrated upstream of the TATA box. The fluorescent proteins included BFP, mCherry, and iRFP713 are used as reporters. UAS nucleotide sequence: 5′-CGGAGTACTGTCCTCCGAGCGGAGTACTGTCCTCCGAGCGGAGTACTGTCCTCCGAGCGGAGTACTGTCCTCCGAGCGGAGTACTGTCCTCCGAG-3′. AP-box nucleotide sequence: 5′-TGAGTCAGTGACTCAGTGAGTCAGTGACTCAGTGAGTCAGTGACTCAGTGAGTCAGTGACTCA-3′. E-box nucleotide sequence: 5′-CACGTGAGCACGTGAGCACGTGTCCACGTGCCCGCACACGTGTCCACGTGCACACGTG-3′.

Materials

Dulbecco's Modified Eagle Medium (DMEM, cat. no. G4524-500ML) and 1× Phosphate-Buffered Saline (PBS) and 1× Dulbecco's phosphate-buffered saline (DPBS, cat. no. G4202-500ML) were acquired from Servicebio. Fetal Bovine Serum (FBS, cat. no. 04-001-1ACS) was procured from Biological Industries. Penicillin-Streptomycin (100×) (P/S, cat. no. C40100) was obtained from New Cell & Molecular Biotech Co. Ltd. Triton X-100 (cat. no. A110694, CAS: 9002-93-1) was purchased from Sangon. The 0.25% Trypsin-EDTA (1×) solution (cat. no. 25200072) was purchased from Thermo Fisher Scientific. JetPRIME® (Polyplus Transfection, cat. no. 041047583) was sourced from Titan. Chemical compounds including Rapamycin (Sigma-Aldrich, cat. no. 37094, CAS: 53123-88-9), ABA (Sigma-Aldrich, cat. no. 862169, CAS: 14375-45-2), GW1929 (TargetMol, cat. no. TQ0156, CAS: 196808-24-9), Rosiglitazone (Energy Chemical, cat. no. A0506760010, CAS: 122320-73-4), GW9662 (Bidepharm, cat. no. BD317085, CAS: 205827-96-9), Vasopressin (from Aladdin, cat. no. A302232, CAS: 113-79-1), and lixivaptan (Sigma-Aldrich, cat. no. SML0603, CAS: 168079-32-1) were initially solubilized in dimethyl sulfoxide (DMSO) at concentrations of either 1 mM, 10 mM or 100 mM. Alkaline Phosphatase Assay (SEAP) kit (cat. no. P0321M) was purchased from Beyotime (Shanghai, China). IL-2 (abs510001), IFN-γ (abs510007) ELISA kit were purchased from Absin Bioscience Inc (Shanghai, China). Pyroptosis detection kit (cat. no. 40304ES60) was purchased from YEASEN (Shanghai, China). LDH detection kit (cat. no. J2380) was purchased from Promega (Beijing, China). For the purpose of cellular stimulation, these molecules were subsequently diluted in DMEM supplemented with 10% FBS and 1% Penicillin-Streptomycin, to achieve the desired final concentration. The cellular cultures were treated with the small-molecule inducers 24 h subsequent to transfection. Primary antibodies used: Anti-Flag: Cell Signaling Technologies cat. no. 14793. Secondary antibodies used: Alexa Fluor 555-Labeled Donkey Anti-Rabbit IgG: Beyotime cat. no. P0179; Goat Anti-Rabbit IgG H&L: Vazyme cat. no. Ab207.

Cell culture and transfection

HEK293T, NIH3T3, HeLa, and MCF-7 cells were cultured in DMEM supplemented with 10% (volume/volume) fetal bovine serum (FBS), alongside 100 units/mL of penicillin and 100 µg/mL of streptomycin, at a constant temperature of 37 °C in a humidified environment that maintained a 5% CO_2 concentration. Jurkat T-cell was cultured in RPMI 1640 medium supplemented with 10% FBS at 37 °C in 5% CO_2. These cells were plated onto sterilized glass coverslips positioned in 35 mm dishes featuring 14 mm wells and within 24-well plates, and were kept at 37 °C in a humidified atmosphere containing 5% CO_2. The cells were transfected with a mixture of plasmids and jetPRIME transfection reagent according to a specific ratio (1 µg of plasmids to 2 µL of jetPRIME, within a total volume of 100 µL of jetPRIME Buffer), adhering to the guidelines provided by the manufacturer. After a 4-h transfection period, these cells were cultivated in a complete medium.

To optimize eGAL-derived PRCIS, eGAL$^{o/+}$, eGAL$^{+/o}$, eGAL$^{-/+}$, eGAL$^{+/-}$ or eGAL$^{+/+}$ were co-transfected with a UAS-TATA-mCherry reporter plasmid, along with BFP-TEVp (BFP for the comparison group) at a ratio of 1:1:1 (100 ng:100 ng:100 ng in a 24-well plate, 300 ng:300 ng:300 ng in a 35 mm confocal dish). To report chemical inputs by eGAL$^{+/+}$, FKBP-nTEVp-eGAL$^{+/+}$ were mixed with FRB-cTEVp and corresponding reporter plasmid at a ratio of 1:1:1. To examine the performance of the eGAL$^{+/+}$ activation within the MESA system, FKBP-nTEVp-GAL4(1-147) or FKBP-

nTEVp-eGAL$^{+/+}$ was cotransfected with FRB-cTEVp, UAS-TATA-mCherry and BFP at a ratio of 1:1:10:1 (20 ng:20 ng:200 ng:20 ng in a 24-well plate, 60 ng:60 ng:600 ng:60 ng in a 35 mm confocal dish). To report PPARγ/RXRα, eGAL$^{+/+}$-nTEVp-PPARγ were typically mixed with cTEVp-RXRα and corresponding reporter plasmid at a ratio of 1:1:10. To investigate the reporting of GPCR signaling pathway by eGAL$^{+/+}$, co-transfection of AVPR2 and β-arrestin constructs were performed with plasmids mixed at a ratio of 1:1:10 (β-arrestin2-nTEVp-eGAL$^{+/+}$/AVPR2-cTEVp/reporter). To generalize TEVp-responsive eGAL$^{+/+}$ to TVMVp, HCVp, PPVp, and GCN4, MAX, and MAX/MYC, each PRCIS plasmid, protease plasmid, and mCherry reporter pasmid were transfected at a ratio of 1:1:1. To develop PRCIS-based orthogonal platforms and Boolean operations, the plasmids used in each system were tranfected equivalently.

Live cell imaging

Cells were transfected with reporter and PRCIS plasmids and stimulated with co-expressed proteases or chemicals for reporter activation, and seeded in 35-mm glass-bottom dishes 24 h before imaging, washed with PBS, and incubated in a DMEM (10% FBS, 1% P/S) medium before imaging. All fluorescence images were collected with a Zeiss LSM980 confocal laser scanning microscope using an oil immersion objective lens of ×40, ×100, or a dry objective lens of ×20. Fluorescence images were collected using the following collection channels upon laser excitation (405 nm, 488 nm, 543 nm, 639 nm). Emission Filters: BFP, 425–475 nm; EGFP/split GFP, 491–570 nm; mCherry, 575–625 nm; iRFP, 650–700 nm. Images were processed with ZEN 3.6 software (blue edition).

Flow cytometry analysis

Cells were transfected with reporter and PRCIS plasmids and stimulated with co-expressed proteases or chemicals for reporter activation. After 24 h, the cells were washed three times with PBS (pH = 7.4), detached with trypsin (0.125%), and centrifuged at 252 × *g* for 3 min at room temperature. Then, the pellets were resuspended in PBS for flow cytometric analysis on a FACSCelesta™ flow cytometer (BD Biosciences, USA). More than 10,000 transfected cells (BFP or GFP positive) were collected for analysis. Excitation and Emission Filters: BFP, 405 nm, and 450/50 nm; EGFP/split GFP, 488 nm and 530/30 nm; mCherry, 561 nm, and 610/20 nm; iRFP, 640 nm, and 670/30 nm. The obtained data were processed by FlowJo_V10 software.

Immunofluorescence analysis

Cells were seeded into 35-mm glass-bottom dishes. C-terminal FLAG tagged eGAL$^{+/+}$ or GAL4(1-147) were transfected in the cells, 24 h post transfection, cells were washed with PBS, fixed with 4% paraformaldehyde for 15 min at room temperature, washed thrice, and permeabilized with 0.1% Triton X-100 in PBS for 5 min at 4 °C. Then, cells were incubated with 10% FBS in PBS for 1 h at room temperature. After blocking, cells were incubated with DYKDDDDK Tag (D6W5B) Rabbit antibody (CST, 14793) overnight at 4 °C. After washing with PBS, cells were then incubated with the Alexa Fluor 555-Labeled Donkey Anti-Rabbit IgG (Beyotime, P0179) for 90 min at room temperature. Cells were washed with PBS and incubated with Hoechst for 10 min. The immunostained cells were then imaged with a Zeiss LSM 980 Basic Operation confocal laser scanning microscope equipped with a 63× lens using DAPI (for Hoechst), GFP (for splitGFP) and mCherry (for Alexa Fluor 555) filters. Images were processed using the software ZEN 3.6 (blue edition). The nuclear to cytoplasmic fluorescence ratio (NCR) is calculated as a result of the integrated fluorescence intensity of the nucleous (IFIn) divide the integrated fluorescence intensity of the cytoplasm (IFIc) (**1**):

$$NCR = \frac{IFIn}{IFIc} \quad (1)$$

CUT&Tag analysis

Cells were transfected with C-terminal FLAG tagged eGAL$^{+/+}$ or GAL4(1-147) plasmids. The transfected cells were detached with trypsin (0.125%), and centrifuged at 252×*g* for 3 min at room temperature, and then resuspended in 1×PBS. All samples were stained with trypan blue (0.4%) to ensure cell viability is greater than 90%. 200,000 cells were collected per sample and processed using the CUT & Tag Assay kit (Vazyme, TD904) according to the manufacturer's instructions. The dilution ratio of the DYKDDDDK Tag (D6W5B) Rabbit antibody (CST, 14793) and Goat Anti-Rabbit IgG H&L (Vazyme, Ab207) was 1:50, 1:100, respectively. Ultimately, the libraries were sequenced on Illumina Novaseq v1.0 and carried out by Novogene Corporation (Beijing, China).

CUT&Tag Data analysis was performed using the CUT_Tag_Tool_V2.0 tool. Sequenced reads were aligned to the human reference genome (hg38) using Bowtie2 (v.2.5.3) with the parameters: –very-sensitive-local–no-unal–no-mixed–no-discordant –phred33 -I 10 -X 700. Alignment BAM files were converted to bigwig format using deeptools (v.3.5.1) software and imported into IGV (v.2.19.2) software for visualization. The enrichment of all samples at the TSS site (±5 kb) was combined to contrast the signal intensities across samples. The genome was divided into equal length intervals, for the number of reads in each interval, and the Pearson correlation was calculated by comparing the number of reads between different samples. Peak calling was performed by MACS2 (v.2.2.6) call peak mode with parameters: -t-g–keep-dup=1. The overlapping peaks of all samples were merged into a common peak list, and unique peaks for each sample were placed in the specific peak list. All peaks were filtered with parameter: |log2(FC)| >0.57 & padj <0.05, and then used to plot Venn map.

SEAP quantification

Secreted embryonic alkaline phosphatase (SEAP) levels in the cell culture medium were determined as follows: After 24 h of transfection, 50 μL of the culture supernatant was heat-inactivated for 30 min at 65 °C, and then added to a 96-well plate. Subsequently, 50 μL para-nitrophenyl phosphate solution was added to each well, and reacted at 37 °C for ~10 min. The reaction was terminated by adding 100 μL of the termination solution. Then, the absorbance at 405 nm was measured at 37 °C using a SpectraMax Microplate reader. SEAP concentrations were calculated from a standard curve.

Jurkat T-cell activation assay

Jurkat T-cell activation assay was determined as follows: HEK293T cells were plated in the lower chamber of a 24-well plate. On the following day, cells were transfected with the corresponding plasmids. After 24 h of transfection, Jurkat T-cells were plated and co-cultured with 293 T cells (1:1 ratio) in a 24-well plate for 48 h. Culture supernatant was collected, and the level of IL-2 secretion was measured by ELISA according to the manufacturer's instructions.

Cell pyroptosis assay

After 24 h of transfection, cells were harvested from the culture wells of 24-well plates. To collect all cells, the supernatant containing floating cells was first transferred to a 1.5-mL tube. Then, cells were washed with Dulbecco's phosphate-buffered saline (DPBS) and trypsinized using 0.125% Trypsin (without EDTA) (ThermoFisher) for 5 min at room temperature. Afterwards, the trypsinized cells were pooled with the supernatant and pelleted the cells in a tabletop centrifuge at 300 × *g* for 5 min. Then, cells were resuspended in 100 μL 1× Binding buffer. PI staining solution (10 μL, 20 μg/mL) was added into tube. Cells were mixed gently, avoided light and reacted at room temperature for 15 min. After the reaction, 400 μL of 1× Binding buffer was added, mixed and placed on ice, and samples were detected by flow cytometry within 1 h.

LDH detection assay

Lactate dehydrogenase (LDH) levels in the cell culture medium were determined as follows: After 24 h of transfection, 50 μL of the supernatant was collected, and added to a 96-well plate. Subsequently, 50 μL LDH detection solution was added to each well, and reacted at room temperature for 40 min. The reaction was terminated by adding 50 μL of the termination solution. Then, the absorbance at 490 nm was measured at 37 °C using a SpectraMax Microplate reader. LDH release was calculated using Eq. (2).

$$LDH\ release\,(\%) = 100 \times \frac{Experimental\ LDH\ Release - Medium\ Background}{Maximum\ LDH\ Release\ Control - Medium\ Background} \quad (2)$$

where Experimental LDH release is measured from the experimental group, Medium Background is measured from the only cells control, Maximum LDH release control is measured by adding 2 μL of 10% Triton X-100 per 100 μL to vehicle-only cells for 10-15 min before collecting the samples for LDH detection.

Statistical analysis and graphic illustration

Data are from three replicated experiments and presented as mean ± standard deviation. The significance and statistical graphs were analyzed and plotted by GraphPad Prism using the unpaired two-tailed Student's t-test. Graphic illustrations are created with BioRender.com with permission.

Reporting summary

Further information on research design is available in the Nature Portfolio Reporting Summary linked to this article.

Data availability

The authors declare that all relevant data supporting the findings of this study are available within the paper and its Supplementary Information files. The CUT&Tag data generated in this study have been deposited in the Sequence Read Archive (SRA) database under accession PRJNA1243281. Source data are provided with this paper.

References

1. Chen, Z. & Elowitz, M. B. Programmable protein circuit design. *Cell* **184**, 2284–2301 (2021).
2. Quijano-Rubio, A. et al. De novo design of modular and tunable protein biosensors. *Nature* **591**, 482–487 (2021).
3. Lee, H. N., Mehta, S. & Zhang, J. Recent advances in the use of genetically encodable optical tools to elicit and monitor signaling events. *Curr. Opin. Cell Biol.* **63**, 114–124 (2020).
4. Stanton, B. Z., Chory, E. J. & Crabtree, G. R. Chemically induced proximity in biology and medicine. *Science* **359**, https://doi.org/10.1126/science.aao5902 (2018).
5. Greenwald, E. C., Mehta, S. & Zhang, J. Genetically encoded fluorescent biosensors illuminate the spatiotemporal regulation of signaling networks. *Chem. Rev.* **118**, 11707–11794 (2018).
6. Yoshikawa, M., Yoshii, T., Ikuta, M. & Tsukiji, S. Synthetic protein condensates that inducibly recruit and release protein activity in living cells. *J. Am. Chem. Soc.* **143**, 6434–6446 (2021).
7. Tellechea-Luzardo, J., Stiebritz, M. T. & Carbonell, P. Transcription factor-based biosensors for screening and dynamic regulation. *Front Bioeng. Biotechnol.* **11**, 1118702 (2023).
8. Kipniss, N. H. et al. Engineering cell sensing and responses using a GPCR-coupled CRISPR-Cas system. *Nat. Commun.* **8**, 2212 (2017).
9. Schwarz, K. A., Daringer, N. M., Dolberg, T. B. & Leonard, J. N. Rewiring human cellular input-output using modular extracellular sensors. *Nat. Chem. Biol.* **13**, 202–209 (2017).
10. Morsut, L. et al. Engineering customized cell sensing and response behaviors using synthetic notch receptors. *Cell* **164**, 780–791 (2016).
11. Allen, G. M. et al. Synthetic cytokine circuits that drive T cells into immune-excluded tumors. *Science* **378**, eaba1624 (2022).
12. Teixeira, A. P. & Fussenegger, M. Synthetic gene circuits for regulation of next-generation cell-based therapeutics. *Adv. Sci. (Weinh.)* **11**, e2309088 (2024).
13. Dray, K. E., Edelstein, H. I., Dreyer, K. S. & Leonard, J. N. Control of mammalian cell-based devices with genetic programming. *Curr. Opin. Syst. Biol.* **28**, https://doi.org/10.1016/j.coisb.2021.100372 (2021).
14. Traven, A., Jelicic, B. & Sopta, M. Yeast Gal4: a transcriptional paradigm revisited. *EMBO Rep.* **7**, 496–499 (2006).
15. Kim, M. W. et al. Time-gated detection of protein-protein interactions with transcriptional readout. *Elife* **6**, https://doi.org/10.7554/eLife.30233 (2017).
16. Zhou, J., Ge, Q., Wang, D., Guo, Q. & Tao, Y. Engineering a modular double-transmembrane synthetic receptor system for customizing cellular programs. *Cell Rep.* **42**, 112385 (2023).
17. Manhas, J., Edelstein, H. I., Leonard, J. N. & Morsut, L. The evolution of synthetic receptor systems. *Nat. Chem. Biol.* **18**, 244–255 (2022).
18. To, T. L. et al. Rationally designed fluorogenic protease reporter visualizes spatiotemporal dynamics of apoptosis in vivo. *Proc. Natl. Acad. Sci. USA* **112**, 3338–3343 (2015).
19. Zhou, G., Wan, W. W. & Wang, W. Modular peroxidase-based reporters for detecting protease activity and protein interactions with temporal gating. *J. Am. Chem. Soc.* **144**, 22933–22940 (2022).
20. Zhang, Q. et al. Designing a green fluorogenic protease reporter by flipping a beta strand of GFP for imaging apoptosis in animals. *J. Am. Chem. Soc.* **141**, 4526–4530 (2019).
21. Grawe, A., Ranglack, J., Weber, W. & Stein, V. Engineering artificial signalling functions with proteases. *Curr. Opin. Biotechnol.* **63**, 1–7 (2020).
22. Siciliano, V. et al. Engineering modular intracellular protein sensor-actuator devices. *Nat. Commun.* **9**, 1881 (2018).
23. Dyer, R. P. & Weiss, G. A. Making the cut with protease engineering. *Cell Chem. Biol.* **29**, 177–190 (2022).
24. Vlahos, A. E. et al. Protease-controlled secretion and display of intercellular signals. *Nat. Commun.* **13**, 912 (2022).
25. Gao, X. J., Chong, L. S., Kim, M. S. & Elowitz, M. B. Programmable protein circuits in living cells. *Science* **361**, 1252–1258 (2018).
26. Xia, S. et al. Synthetic protein circuits for programmable control of mammalian cell death. *Cell* **187**, 2785–2800 e2716 (2024).
27. Chung, H. K. et al. A compact synthetic pathway rewires cancer signaling to therapeutic effector release. *Science* **364**, https://doi.org/10.1126/science.aat6982 (2019).
28. Baeumler, T. A., Ahmed, A. A. & Fulga, T. A. Engineering synthetic signaling pathways with programmable dCas9-based chimeric receptors. *Cell Rep.* **20**, 2639–2653 (2017).
29. Dickinson, B. C., Packer, M. S., Badran, A. H. & Liu, D. R. A system for the continuous directed evolution of proteases rapidly reveals drug-resistance mutations. *Nat. Commun.* **5**, 5352 (2014).
30. Noviello, G., Gjaltema, R. A. F. & Schulz, E. G. CasTuner is a degron and CRISPR/Cas-based toolkit for analog tuning of endogenous gene expression. *Nat. Commun.* **14**, 3225 (2023).
31. Marmorstein, R., Carey, M., Ptashne, M. & Harrison, S. C. DNA recognition by GAL4: Structure of a protein-DNA complex. *Nature* **356**, 408–414 (1992).
32. Hong, M. et al. Structural basis for dimerization in DNA recognition by Gal4. *Structure* **16**, 1019–1026 (2008).
33. Wang, X., Chen, X. & Yang, Y. Spatiotemporal control of gene expression by a light-switchable transgene system. *Nat. Methods* **9**, 266–269 (2012).
34. Redchuk, T. A., Omelina, E. S., Chernov, K. G. & Verkhusha, V. V. Near-infrared optogenetic pair for protein regulation and spectral multiplexing. *Nat. Chem. Biol.* **13**, 633–639 (2017).

35. Liang, F. S., Ho, W. Q. & Crabtree, G. R. Engineering the ABA plant stress pathway for regulation of induced proximity. *Sci. Signal* **4**, rs2 (2011).
36. De Crescenzo, G., Litowski, J. R., Hodges, R. S. & O'Connor-McCourt, M. D. Real-time monitoring of the interactions of two-stranded de novo designed coiled-coils: effect of chain length on the kinetic and thermodynamic constants of binding. *Biochemistry* **42**, 1754–1763 (2003).
37. Romei, M. G. & Boxer, S. G. Split green fluorescent proteins: Scope, limitations, and outlook. *Annu Rev. Biophys.* **48**, 19–44 (2019).
38. Bryant, P., Pozzati, G. & Elofsson, A. Improved prediction of protein-protein interactions using AlphaFold2. *Nat. Commun.* **13**, 1265 (2022).
39. Niopek, D. et al. Engineering light-inducible nuclear localization signals for precise spatiotemporal control of protein dynamics in living cells. *Nat. Commun.* **5**, 4404 (2014).
40. Kaya-Okur, H. S. et al. CUT&Tag for efficient epigenomic profiling of small samples and single cells. *Nat. Commun.* **10**, 1930 (2019).
41. Barcenas-Walls, J. R. et al. Nano-CUT&Tag for multimodal chromatin profiling at single-cell resolution. *Nat. Protoc.* **19**, 791–830 (2024).
42. Kane, L. P., Andres, P. G., Howland, K. C., Abbas, A. K. & Weiss, A. Akt provides the CD28 costimulatory signal for up-regulation of IL-2 and IFN-gamma but not TH2 cytokines. *Nat. Immunol.* **2**, 37–44 (2001).
43. Chaisupa, P. & Wright, R. C. State-of-the-art in engineering small molecule biosensors and their applications in metabolic engineering. *SLAS Technol*, https://doi.org/10.1016/j.slast.2023.10.005 (2023).
44. Wang, X. et al. A programmable protease-based protein secretion platform for therapeutic applications. *Nat. Chem. Biol.* **20**, 432–442 (2024).
45. Wehr, M. C. et al. Monitoring regulated protein-protein interactions using split TEV. *Nat. Methods* **3**, 985–993 (2006).
46. Bertschi, A., Wang, P., Galvan, S., Teixeira, A. P. & Fussenegger, M. Combinatorial protein dimerization enables precise multi-input synthetic computations. *Nat. Chem. Biol.* **19**, 767–777 (2023).
47. Daringer, N. M., Dudek, R. M., Schwarz, K. A. & Leonard, J. N. Modular extracellular sensor architecture for engineering mammalian cell-based devices. *ACS Synth. Biol.* **3**, 892–902 (2014).
48. Dolberg, T. B. et al. Computation-guided optimization of split protein systems. *Nat. Chem. Biol.* **17**, 531–539 (2021).
49. Edelstein, H. I. et al. Elucidation and refinement of synthetic receptor mechanisms. *Synth. Biol. (Oxf.)* **5**, ysaa017 (2020).
50. Zhang, M. et al. G protein-coupled receptors (GPCRs): advances in structures, mechanisms, and drug discovery. *Signal Transduct. Target Ther.* **9**, 88 (2024).
51. Barnea, G. et al. The genetic design of signaling cascades to record receptor activation. *Proc. Natl. Acad. Sci. USA* **105**, 64–69 (2008).
52. Chandra, V. et al. Structure of the intact PPAR-gamma-RXR- nuclear receptor complex on DNA. *Nature* **456**, 350–356 (2008).
53. Kilu, W., Merk, D., Steinhilber, D., Proschak, E. & Heering, J. Heterodimer formation with retinoic acid receptor RXRalpha modulates coactivator recruitment by peroxisome proliferator-activated receptor PPARgamma. *J. Biol. Chem.* **297**, 100814 (2021).
54. Fernandez-Rodriguez, J. & Voigt, C. A. Post-translational control of genetic circuits using Potyvirus proteases. *Nucleic Acids Res.* **44**, 6493–6502 (2016).
55. Fink, T. & Jerala, R. Designed protease-based signaling networks. *Curr. Opin. Chem. Biol.* **68**, 102146 (2022).
56. Cella, F., Wroblewska, L., Weiss, R. & Siciliano, V. Engineering protein-protein devices for multilayered regulation of mRNA translation using orthogonal proteases in mammalian cells. *Nat. Commun.* **9**, 4392 (2018).
57. Wolberger, C. How structural biology transformed studies of transcription regulation. *J. Biol. Chem.* **296**, 100741 (2021).
58. Ellenberger, T. E., Brandl, C. J., Struhl, K. & Harrison, S. C. The GCN4 basic region leucine zipper binds DNA as a dimer of uninterrupted alpha helices: crystal structure of the protein-DNA complex. *Cell* **71**, 1223–1237 (1992).
59. Ferre-D'Amare, A. R., Prendergast, G. C., Ziff, E. B. & Burley, S. K. Recognition by Max of its cognate DNA through a dimeric b/HLH/Z domain. *Nature* **363**, 38–45 (1993).
60. Fink, T. et al. Design of fast proteolysis-based signaling and logic circuits in mammalian cells. *Nat. Chem. Biol.* **15**, 115–122 (2019).
61. Makri Pistikou, A. M. et al. Engineering a scalable and orthogonal platform for synthetic communication in mammalian cells. *Nat. Commun.* **14**, 7001 (2023).
62. Lebar, T., Lainscek, D., Merljak, E., Aupic, J. & Jerala, R. A tunable orthogonal coiled-coil interaction toolbox for engineering mammalian cells. *Nat. Chem. Biol.* **16**, 513–519 (2020).
63. Lainscek, D. et al. Coiled-coil heterodimer-based recruitment of an exonuclease to CRISPR/Cas for enhanced gene editing. *Nat. Commun.* **13**, 3604 (2022).
64. Rondon, R. E., Groseclose, T. M., Short, A. E. & Wilson, C. J. Transcriptional programming using engineered systems of transcription factors and genetic architectures. *Nat. Commun.* **10**, 4784 (2019).
65. Nakamura, M. et al. Anti-CRISPR-mediated control of gene editing and synthetic circuits in eukaryotic cells. *Nat. Commun.* **10**, 194 (2019).
66. Kleinjan, D. A., Wardrope, C., Nga Sou, S. & Rosser, S. J. Drug-tunable multidimensional synthetic gene control using inducible degron-tagged dCas9 effectors. *Nat. Commun.* **8**, 1191 (2017).

Acknowledgements

This work was supported by the NSFC Programs (Grant 22204046, J.H.), the National Key Research Program (Grant 2019YFA0905800, J.H., and J.H.J.), the Hunan Science Fund for Excellent Young Scholars (2023JJ20002, J.H.), and the Science and Technology Major Project of Hunan Province (2021SK1020, Y. Long, J.H., and J.H.J.).

Author contributions

Y.Liu and L.Z. designed the plasmid constructs, Y.Liu and J.L. performed the fluorescence imaging and flow cytometry experiments. Z. H. performed the Alphafold2 stimulation. Y.Liu, J.H., and J.H.J. designed and analyzed the experiments and wrote the manuscript. J.H. and J.H.J. conceived the study. Y. Long, J.H., and J.H.J. supervised this study.

Competing interests

The authors declare no competing interests.

Additional information

Supplementary information The online version contains supplementary material available at https://doi.org/10.1038/s41467-025-59828-6.

Correspondence and requests for materials should be addressed to Jianjun He or Jian-Hui Jiang.

Peer review information *Nature Communications* thanks Ye Chen and the other, anonymous, reviewer(s) for their contribution to the peer review of this work. A peer review file is available.